

Bond relaxation and electronic properties of T-type WTe₂/MoS₂ heterostructure using BOLS BB and BC model

Hongrong Qiu, Hanze Li, Jiannan Wang, Yunhu Zhu, Maolin Bo*

Key Laboratory of Extraordinary Bond Engineering and Advanced Materials Technology (EBEAM) of Chongqing, Yangtze Normal University, Chongqing 408100, China

Corresponding Author: *E-mail: bmlwd@yznu.edu.cn (Maolin Bo)

Abstract

We combined the bond-order-length-strength (BOLS) binding energy(BB) and bond charge (BC) models and the topological concept to obtain the nonbonding, bonding, and antibonding states of the T-type WTe₂/MoS₂ heterostructure. We found that the electronic probability and electronic dispersion in the valence band of the WTe₂/MoS₂ heterostructure can be determined precisely based on electronic entropy. The energy-band projection method and electronic entropy are remarkable approaches for analyzing the electronic properties of various structures based on DFT calculations. This study provides a new way to describe the electronic properties of T-type heterostructures and calculate the electron and bonding state probabilities.

Key words: electronic properties, T-type heterostructure, WTe₂/MoS₂, DFT calculation, bond relaxation

1. Introduction

Two-dimensional transition metal sulfides (TMDs) have attracted considerable attention due to their advantageous properties, such as high current-carrying mobility and wide adjustable band gap.^[1-3] TMDs are used in many applications, including semiconductor devices and photocatalysis.^[4] TMDs have a sandwich-like structure, with a transition metal element layer in the middle and two chalcogen elements on both sides.^[5] Different kinds of TMDs materials have different electrical and optical properties,^[6] and specific properties can be obtained by forming TMDs heterostructures.^[7] By growing MoSe₂/WSe₂ heterostructures, excitons can be formed in the MoS₂/MoSe₂ heterostructure, and the interlayer interaction of the MoS₂/WS₂ heterostructure can be observed. Ullah et al. investigated the growth of MoSe₂/WSe₂ lateral heterostructures.^[8] Ceballos et al. reported the formation of long-lived indirect excitons in an MoS₂-MoSe₂ heterostructure.^[9] Yelgel et al. showed the WS₂/MoS₂ heterostructure has a stable structure and excellent electronic properties.^[10] The results of these studies suggest that the formation of a two-dimensional TMDs heterostructure may change the electronic state, and form the excitons, allowing their application in various devices.^[11] Most two-dimensional TMDs heterostructures are stacked into different shapes and connected by van der Waals forces between layers.^[12] However, there are few studies on vertical heterojunctions connected by chemical bonds. In optoelectronic devices, vertical heterojunctions can better satisfy electron migration and provide a larger working area for optoelectronic devices.^[13] Therefore, we studied the T-type heterostructure of WTe₂/MoS₂.

In this study, we constructed a T-type WTe₂/MoS₂ heterostructure and modeled its structure using density functional theory (DFT) calculations.^[14] Then, we investigated bond relaxation and electronic properties of the T-type WTe₂/MoS₂ heterostructure using the energy-band projection method. In particular, we analyzed the density of state (DOS) and band structure in each energy range along each Brillouin path. We used the concept of electronic entropy to express the electronic dispersion in the valence band of the T-type WTe₂/MoS₂ heterostructure. This energy-band projection method

and the concept of electronic entropy provide a new approach to study the electronic properties of various structures.

2. Methods

2.1 DFT calculation

We aimed to analyze the energetics, electronic properties and the atomic structure of the T-type WTe₂/MoS₂ heterostructure. All structural relaxation and electronic properties of the WTe₂/MoS₂ heterostructure were calculated by CASTEP.^[15] We used the HSE06 hybrid density function to describe the electron exchange and correlation potential;^[16] the cut-off energy was set to 650 eV, and $3 \times 2 \times 1$ k -point grids were used. In the calculations, the energy converged to 10^{-6} eV, and the force on each atom converged to <0.01 eV/Å.

2.2 BOLS- BB model

The Hamiltonian is given by

$$H = \left[-\frac{\hbar^2 \nabla^2}{2m} + V_{atom}(r) \right] + V_{cry}(r)(1 + \Delta_H) \quad (1)$$

$V_{atom}(r)$ is the intra-atomic potential of the atom, $V_{cry}(r)$ is the potential of the crystal, and the interaction potential changes with the coordination environment and during chemical reactions. The electronic binding energy (BE) of the ν th energy band $E_\nu(0)$ and $E_\nu(B)$ are

$$E_\nu(0) = -\langle v, i | -\frac{\hbar^2 \nabla^2}{2m} + V_{atom}(r) | v, i \rangle \quad (2)$$

$$E_\nu(x) - E_\nu(0) = -\alpha_\nu - \sum_j f(k) \cdot \beta_\nu = -\alpha_\nu (1 + \sum_j \frac{f(k) \cdot \beta_\nu}{\alpha_\nu}) \cong -\alpha_\nu (1 + \Delta_H) \propto \langle E_x \rangle \quad (3)$$

The $E_v(x)$ and $E_v(0)$ are the energy levels of atoms and an isolated atom, respectively. The α_v and β_v contributes to the width of the energy band. In the localized band of core levels, β_v is very small, so α_v determines the energy band of the core levels.

$$\alpha_v = -\langle v, i | V_{cry}(r) | v, i \rangle \propto \langle E_b \rangle$$

$$\beta_v = -\langle v, i | V_{cry}(r) | v, j \rangle; \sum_j f(k) \beta_v \propto \langle E_x - E_b \rangle$$
(4)

The $|v, i\rangle$ represents the wave function. The periodic factor $f(k)$ is the form of e^{ikr} , while k is the wave vector. The β is dependent on the overlap between orbitals centered at two neighboring atoms.

The bond energy E_x uniquely determines the core-level BE shift:^[17]

$$z_x = \frac{12}{\left\{ 8 \ln \left(\frac{2\Delta E'_v(x) - \Delta E_v(B)}{\Delta E_v(B)} \right) + 1 \right\}} \quad (\Delta E_v(x) \geq 0)$$
(5)

where z_x is the atomic coordination number of an atom in the x th atomic layer from the surface.

$$\frac{\Delta E_v(x)}{\Delta E_v(B)} = \frac{\Delta E'_v(x) + \Delta E_v(B)}{\Delta E_v(B)}$$
(6)

$$\frac{\Delta E_v(w_x)}{\Delta E_v(w_B)} \propto \frac{E_x}{E_b} = \gamma = 1 + \Delta_H = c_x^{-m} = \left(\frac{d_x}{d_b} \right)^{-m}$$
(7)

$$\frac{\Delta E_v(w_x)}{\Delta E_v(w_B)} \cong \frac{\Delta E'_v(x) + \Delta E_v(B)}{\Delta E_v(B)} = \gamma \quad (8)$$

$$\Delta V_{cry}(r) = V_{cry}(r)(1 + \Delta_H) = \gamma V_{cry}(r) = (Z+1) \frac{1}{4\pi\epsilon_0} \sum_i \langle v, i | \frac{e^2}{r_i} | v, i \rangle \quad (9)$$

$$E_v(x) - E_v(0) \cong -\langle v, i | V_{cry}(r)(1 + \Delta_H) | v, i \rangle = -(Z+1) \frac{1}{4\pi\epsilon_0} \sum_i \langle v, i | \frac{e^2}{r_i} | v, i \rangle \quad (10)$$

Z is the initial atom charge (neutral $Z = -1$ (isolated atom), positively $Z = 0$ (bulk atoms), positively $Z = +|\delta\gamma|$ ($\gamma > 0$) (charged positive atoms) and negatively $Z = -|\delta\gamma|$ ($\gamma < 0$) (charged negative atoms). Thus the core-electron BE shifts will be 0,

$$-\sum_i \langle v, i | \frac{(1+|\delta\gamma|)}{4\pi\epsilon_0} \frac{e^2}{r_i} | v, i \rangle, -\sum_i \langle v, i | \frac{1}{4\pi\epsilon_0} \frac{e^2}{r_i} | v, i \rangle, -\sum_i \langle v, i | \frac{(1-|\delta\gamma|)}{4\pi\epsilon_0} \frac{e^2}{r_i} | v, i \rangle \quad \text{and} \quad \text{initially}$$

neutral of isolated atom, bulk atoms, singly charged positive and negative atoms, respectively.^[18] **Eq. 7** provides estimates for the bond energy E_x , bond length d_x and

$\Delta E_v(w_B) \cong \Delta E_v(B)$ is the spectral full width of the bulk component (w_B) of the v th energy level; The width of the BE shift for the surface component (w_x) of the v th energy level is $\Delta E_v(w_x) = \Delta E_v(w_B) + \Delta E'_v(x)$; actual spectral intensities and shapes, however, are subject to polarization effects and measurement artifacts. We can calculate the chemisorption and defect-induced interface bond energy ratio γ with the known reference value of $\Delta E'_v(x) = E_v(x) - E_v(B)$, $\Delta E_v(B) = E_v(B) - E_v(0)$ and $\Delta E_v(x) = E_v(x) - E_v(0)$ derived from the surface via DFT calculations and XPS analysis.

Hence, we obtain

$$\delta\gamma = \frac{\Delta E'_v(x)}{\Delta E'_v(w_B)} = \frac{\Delta E'_v(x) + \Delta E'_v(B)}{\Delta E'_v(B)} - 1 = \gamma - 1 \quad (\text{RBER}) \quad (11)$$

$$\delta\varepsilon_x = d_x / d_b - 1 = \gamma^{-1} - 1 \quad (\text{RLBS}) \quad (12)$$

$$\delta E_d = (E_i / d_i^3) / (E_b / d_b^3) - 1 = \gamma^4 - 1 \quad (\text{RBED}) \quad (13)$$

$$\Delta E'_v(x) \cong -\delta\gamma \langle v, i | V_{cry}(r) | v, i \rangle \cong -\sum_j f(k) \langle v, i | V_{cry}(r) | v, j \rangle \propto \langle E_x - E_b \rangle \quad (14)$$

Thus, one can drive the interface binding energy ratio (RBER) parameter $\delta\gamma$. If $\delta\gamma < 0$, the binding energy is reduced, the potential of the crystal and the bond is weakened. Conversely, if $\delta\gamma > 0$, the binding energy increases, the potential of the crystal and the bond becomes stronger. The relative local bond strain (RLBS) $\delta\varepsilon_x$ indicates the relative contraction of the atomic bond length d_x . The relative bond energy density (RBED) δE_d is the energy density of the atomic bond with energy E_i .

3. Results and discussion

3.1 Electronic properties of T-type WTe₂/MoS₂ heterostructure

We obtained the electronic and structural properties of the heterostructure via DFT calculations. As is shown in **Fig. 1**, the structure of the T-type WTe₂/MoS₂ heterostructure. It can be seen from the figure that the structure is T-shaped. The lattice parameters of the T-type WTe₂/MoS₂ heterostructure are presented in **Table 1** ($a = 6.235 \text{ \AA}$, $b = 12.980 \text{ \AA}$, $c = 14.638 \text{ \AA}$), and the optimized atomic coordinate results are presented in **Table 2**. The band structure of the WTe₂/MoS₂ heterostructure is shown in **Fig. 2**. The band gap of the T-type WTe₂/MoS₂ is 0.328 eV. This structure has an indirect band gap. In addition, we observed a flat band in the band gap of the WTe₂/MoS₂ heterostructure. In **Fig. 2**, a very distinct horizontal band with almost no

dispersion appears when the Fermi level ($E_f = 0$) is near zero. It can be concluded that the flat band can adjust the electron states of the band structure.

The total DOS of the T-type $\text{WTe}_2/\text{MoS}_2$ heterostructure is shown in the **Fig. 3**. It can be seen from the figure that the zero domain appears Fermi level ($E_f = 0$). The **Fig. 3** also presents the electronic distribution of the valence band maximum (VBM) of the T-type $\text{WTe}_2/\text{MoS}_2$ heterostructure has an energy of 0 eV and is mainly distributed on the Fermi level. The electron in the conduction band minimum (CBM) is at an energy of approximately 0.015 eV. The PDOS are shown in **Fig. 4**. From the PDOS, we can see that there is a peak at -0.236 eV in the electron density distribution near the Fermi level in the valence band, and a peak at 0.673 eV in the conduction band. We calculate the atomic local DOS of the $\text{WTe}_2/\text{MoS}_2$ heterojunction of Mo ($4p4d5s$), S ($3s3p$), W ($6s5d$) and Te ($5s5p$) atoms. As shown in **Fig. 5**, the $\text{WTe}_2/\text{MoS}_2$ heterostructure of main electron contributions to the conduction band come from the Mo $4d$ and S $3p$ orbitals. Moreover, the W and Te atoms have less electron contribution to the Fermi level.

3.2 Energy-band projection method

We used a new method to analyze the energy distribution near the Fermi surface of the T-type $\text{WTe}_2/\text{MoS}_2$ heterostructure. Also, we can use this method to analyze the probability of electrons appearing in various energy ranges along each Brillouin path. In the following article, I will use electronic entropy to explain the reason. First, we normalized the DOS,^[19] extracted the points with energy between -3 eV and 3 eV in the DOS, and listed the extracted energy as the basis; at the same time, we extracted the energy points and equally divided the corresponding points into 3000 points; after the equalization, the point sequence was integrated and normalized. Second, we stratified the normalized DOS. The point list was integrated piecewise, sorted with a unit of 0.2 eV, and divided into 11 levels (-3 eV \sim 3 eV). Different levels are represented by different colors for probability of electrons. Then, we conducted hierarchical processing on the band structure. The points with energy between -3 eV and 3 eV, and the corresponding data were extracted completely and

the energy range obtained in the second step was matched with the color. The difference between Energy-band projection method and the Fatband software for 2D band projection, is that the Fatband software using the K -point projection,^[20] while Energy-band projection method take the energy projection for subsequent analyses.

Fig. 6 is displayed in a flow picture of the projection, DOS is projected on the band structure diagram based on energy, and different colors are used to represent the electron probabilities. According to Shannon, for a discrete probability distribution, the entropy is defined as follows:^[21]

$$H(X) = - \sum_{x_i \in X} P(x_i) \log P(x_i). \quad (15)$$

For the entropy of electrons, the random variable X represents the energy range corresponding to the point on the path of the Brillouin region, x_i represents one of the energy ranges, $P(x_i)$ represents the probability of the electron appearing in a certain energy range. The electronic entropy corresponding to each energy range can be obtained using the data displayed in **Table 3**. Near the valence band ($-3 \text{ eV} \sim 0 \text{ eV}$), the electron entropy was 0.116 bit. The entropy near the shallow energy level of the valence band ($-0.6 \text{ eV} \sim 0 \text{ eV}$) was calculated to be 0.018 bit. And the conduction band ($0 \text{ eV} \sim 3 \text{ eV}$), the electron entropy was 0.090 bit. The entropy near the shallow energy level of the conduction band ($0 \text{ eV} \sim 1.2 \text{ eV}$) is 0.013 bit.

The order of the electronic entropy values in each range was consistent with the order of the corresponding electron appearance probability. In **Fig. 7**, the energy band structure of the processed DOS projection. Therefore, we can see that the color is closer to black (0 bit), the smaller the entropy value, the smaller the probability of electrons appearing, and the color is closer to red (0.055 bit), the greater the entropy value, and the greater the probability of electrons appearing. It can be clearly seen that around the Fermi level, especially the energy range of the valence band is -0.6 eV to 0 eV , the probability of the occurrence of electrons is generally low. This indicates that the shallow energy level of the valence band is very close to the cavitation-bound state of the valence band in the range of -0.6 eV to 0 eV . The electrons or holes in the shallow

energy level of the valence band are ionized at a slightly higher temperature (e.g., room temperature) to become free electrons in the conduction band and free holes in the valence band, which promote the conduction of electricity.

3.3 Bonding states of T-type WTe₂/MoS₂ heterostructure

We considered a free quantum particle of charge e . We confined the charge e in one dimension and subjected it to periodic boundary conditions, i.e., a particle on a ring. Thus, the free Hamiltonian of the system takes the following forms:^[22]

$$\left\{ \begin{array}{l} H = -\frac{\hbar^2}{2m} \left(\nabla - \frac{q}{\hbar c} A(\vec{r}) i \right)^2 \\ \quad = \frac{1}{2} \left(-i\partial_\phi - A(\vec{r}) \right)^2 \quad (e = 1, \hbar = 1, c = 1), \\ \psi_n(\phi) = \frac{1}{\sqrt{2\pi}} \exp(in\phi), \end{array} \right. \quad (16)$$

where \hbar is Planck's constant, q is the amount of charge, c is the speed of light, \vec{r} is the radius of the electron, and ϕ is the field.

To understand a particle on a ring, we express the field ϕ as mapping

$$\phi: S_1 \rightarrow S_1, \quad \tau \rightarrow \phi(\tau),$$

from the unit circle S_1 into another circle. Mappings of this type can be assigned to a winding number W (see **Fig. 8**). The number of times $\phi(\tau)$ winds around the unit circle as τ progresses from 0 to β : $\phi(\beta) - \phi(0) = 2\pi W$. Here, we noted that the $A(\vec{r})$ -dependent term in the action,

$$S_{top}[\phi] \equiv iA(\vec{r}) \int_0^\beta d\tau \dot{\phi} = iA(\vec{r})(\phi(\beta) - \phi(0)) = i2\pi W A(\vec{r}). \quad (17)$$

Only the index of topological sector ϕ . S_{top} is the topological sector of the field contribution.

The atomic bond relaxation is expressed based on the BOLS-BB model as follows:^[23]

$$E_i \propto V_{cry}(\vec{r}_{ij}) = qA(\vec{r}_{ij}) = qS_{top}[\phi] / i2\pi W$$

(18)

$$\Delta E'_v(x) \cong -\sum_j f(k) \langle v, i | qA(\vec{r}_{ij}) | v, j \rangle = -\sum_j f(k) \langle v, i | qS_{top}[\phi] / i2\pi W | v, j \rangle \propto \Delta E_i$$

(19)

$$\frac{E_i}{E_B} = \left(\frac{1/d_i}{1/d_B} \right)^m \propto \frac{V_{cry}(r_{ij})}{V_{cry}(r_B)} = \gamma; \begin{cases} \gamma > 1, \text{deepening the potential well} \\ \gamma < 1, \text{strengthening the potential Energy Barrier} \end{cases}$$

(20)

Then,

$$V_{cry}(r_{ij}) = \frac{1}{4\pi\epsilon_0} \iiint d^3r_{ij} \iiint d^3r_{ij} \frac{\Delta\rho_{hole}(r_{ij})\Delta\rho_{electron}(r_{ij})}{r_{ij}},$$

(21)

where E_i is the single bond energy, $\Delta\rho(r_{ij})$ is the deformation charge density, d_i is the bond length of the atom, $V_{cry}(r_{ij})$ is the crystal potential, B represents bulk atoms, and m is the bond nature indicator. In **Eq. 18 and 19**, chemical bonds are associated with the topological effects and quantum fields. In **Eq. 20**, the potential function $\gamma V_{cry}(r_{ij})$ may become deeper ($\gamma > 1$) or shallower ($\gamma < 1$) than the corresponding $V_{cry}(r_B)$ of the specific constituent. **Eq. 21** describes the relationship between the deformation charge density $\Delta\rho(r_{ij})$ and the crystal potential $V_{cry}(r_{ij})$. This method has been applied to a variety of structures such as two-dimensional Sb/MoSe₂ and BN/SiC vdW heterostructures.^[23, 24]

Fig. 9 was depicted the deformation charge density. We believe that the formation of the WTe₂/MoS₂ heterostructure is mainly due to the contributions of bonds, electrons, and charges.^[25] Using **Eq. 19**, we calculated crystal potentials of the antibonding states, nonbonding states and bonding states of WTe₂/MoS₂ heterostructure.^[26] **Table 4** presents the electronic states of the three chemical bonds calculated by DFT calculations. The nonbonding states, bonding states, and antibonding states were displayed in the deformation charge density. The dark-red area indicates the bonding state. The light-red area is a nonbonding state. The white area represents the

antibonding state. Furthermore, we analyzing the deformation charge density to definite the atomic bonding information.

4. Conclusion

We used DFT to calculate the constructed T-typed $\text{WTe}_2/\text{MoS}_2$ heterostructure and combined the BOLS-BC model and the topological concept to obtain the nonbonding state, bonding state, and antibonding state of the T-typed $\text{WTe}_2/\text{MoS}_2$ heterostructure. Furthermore, the energy band projection method was used to study the electronic properties of the $\text{WTe}_2/\text{MoS}_2$ heterostructure. Using the formula of electronic entropy, the valence band ($-3 \text{ eV} \sim 0 \text{ eV}$); the shallow energy level of the valence band ($-0.6 \text{ eV} \sim 0 \text{ eV}$); the conduction band ($0 \text{ eV} \sim 3 \text{ eV}$) and the shallow energy level of the conduction band ($0 \text{ eV} \sim 1.2 \text{ eV}$) were calculated to represent the electronic probability of the $\text{WTe}_2/\text{MoS}_2$ heterostructure, respectively. The energy-band projection method and the concept of electronic entropy provide a new approach for studying the electronic properties of various structures.

Acknowledgment

The Scientific and Technological Research Program of Chongqing Municipal Education Commission (KJQN201901424), the Chongqing Natural Science Foundation project (cstc2020jcyjmsxmX0524)

Figure and Table Captions

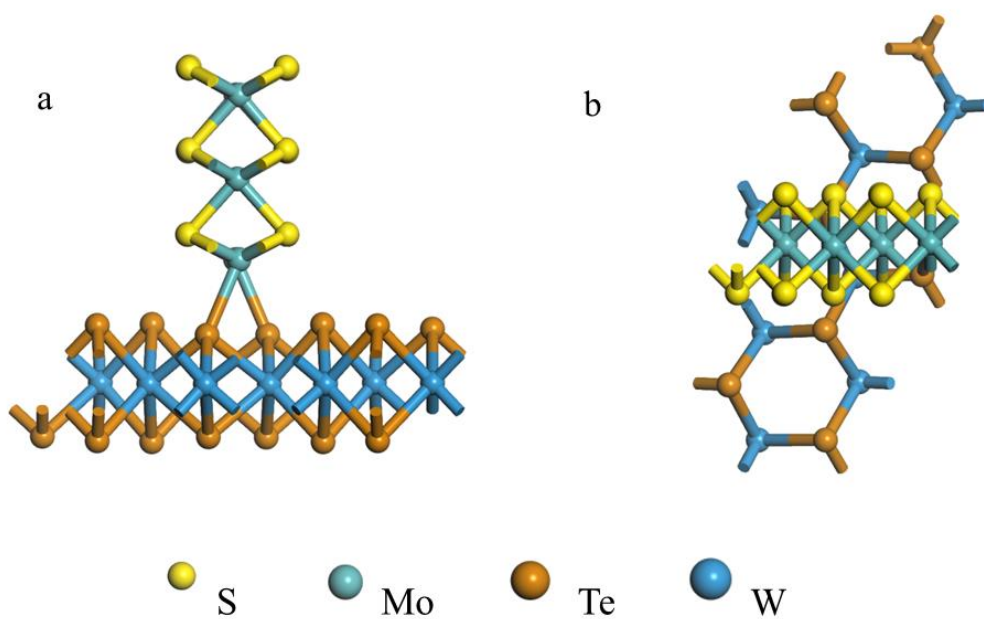


Fig. 1 Front view (a) and top view (b) of T-type WTe_2/MoS_2 heterostructure. Yellow, green, orange, and blue balls represent sulfur, molybdenum, tellurium, and tungsten atoms, respectively.

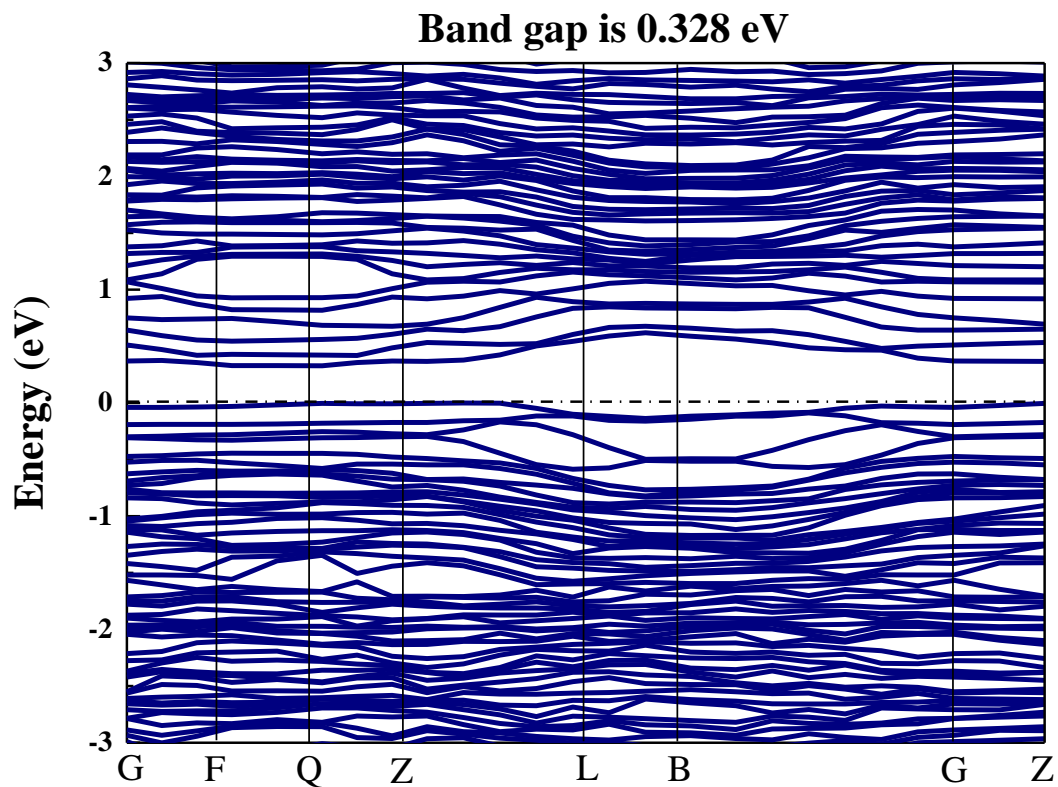


Fig. 2 Band structure of T-type WTe_2/MoS_2 heterostructure

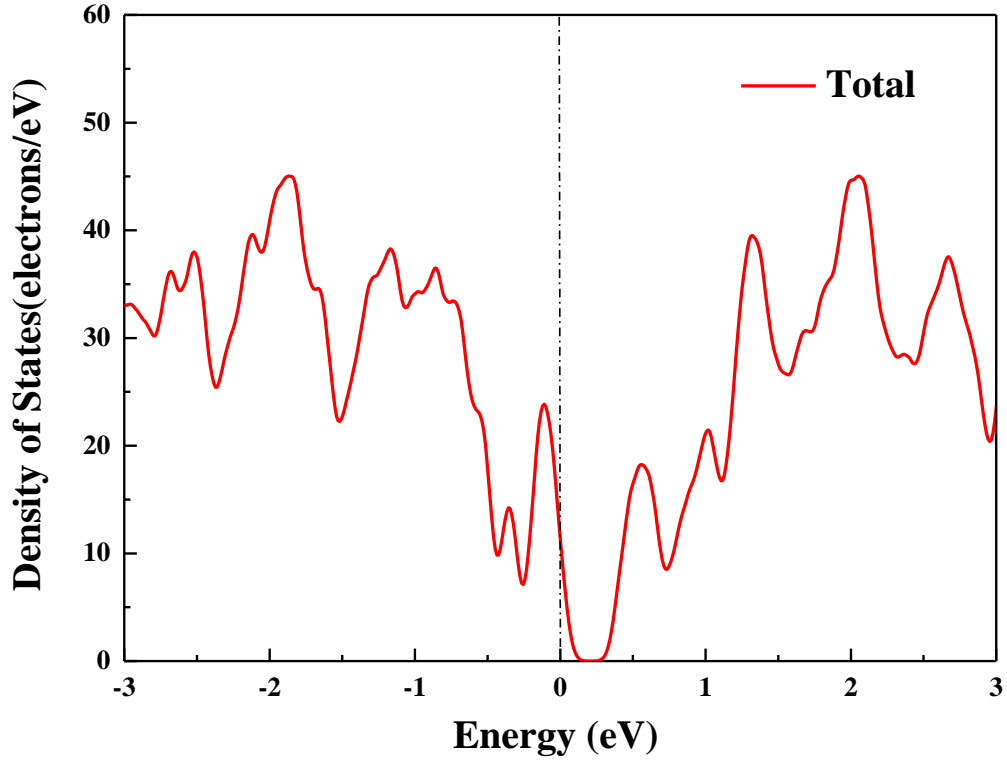


Fig. 3 Total density of states of T-type $\text{WTe}_2/\text{MoS}_2$ heterostructure

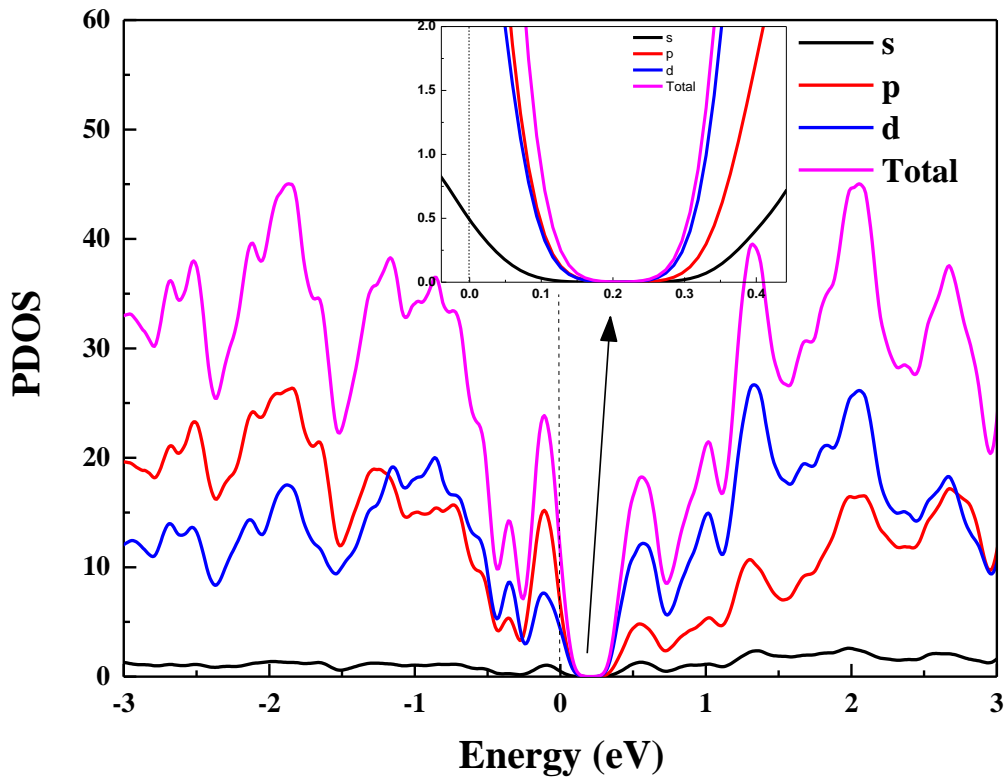


Fig. 4 Partial density of states (PDOS) of T-type $\text{WTe}_2/\text{MoS}_2$ heterostructure

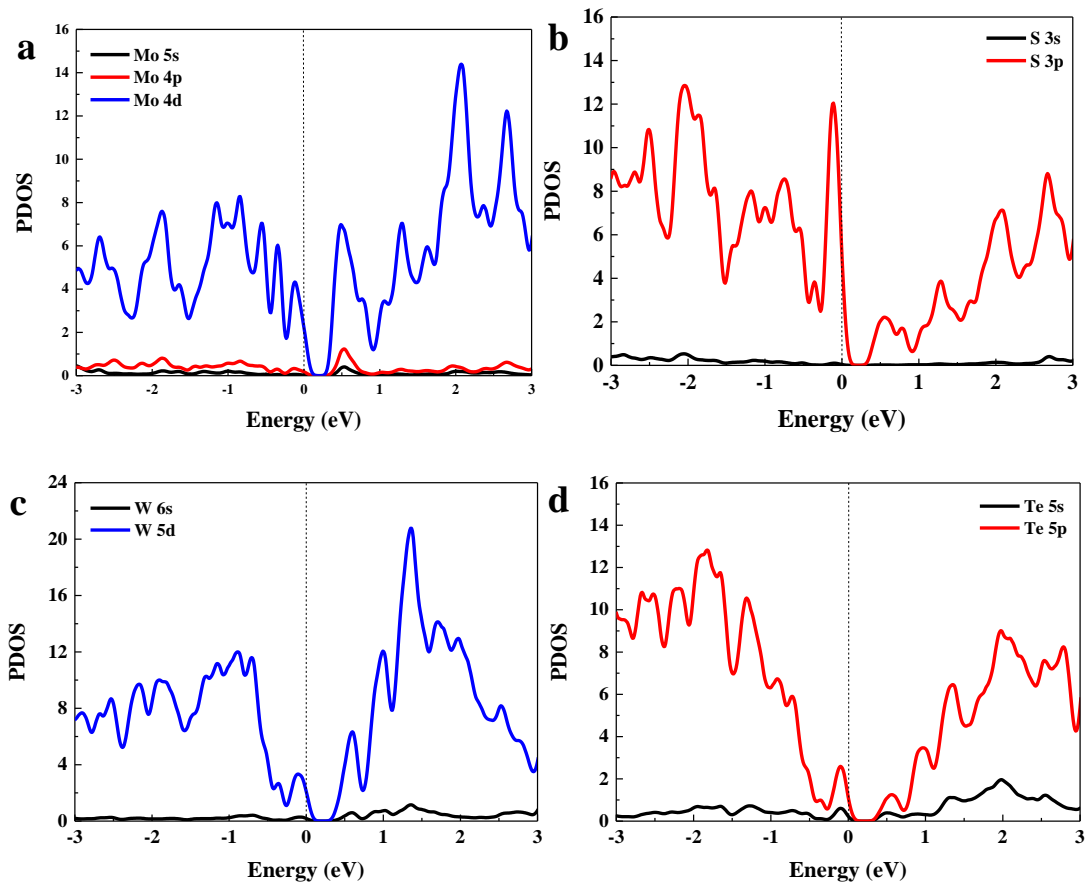


Fig. 5 Partial density of states (PDOS) of Mo, S, W and Te atoms

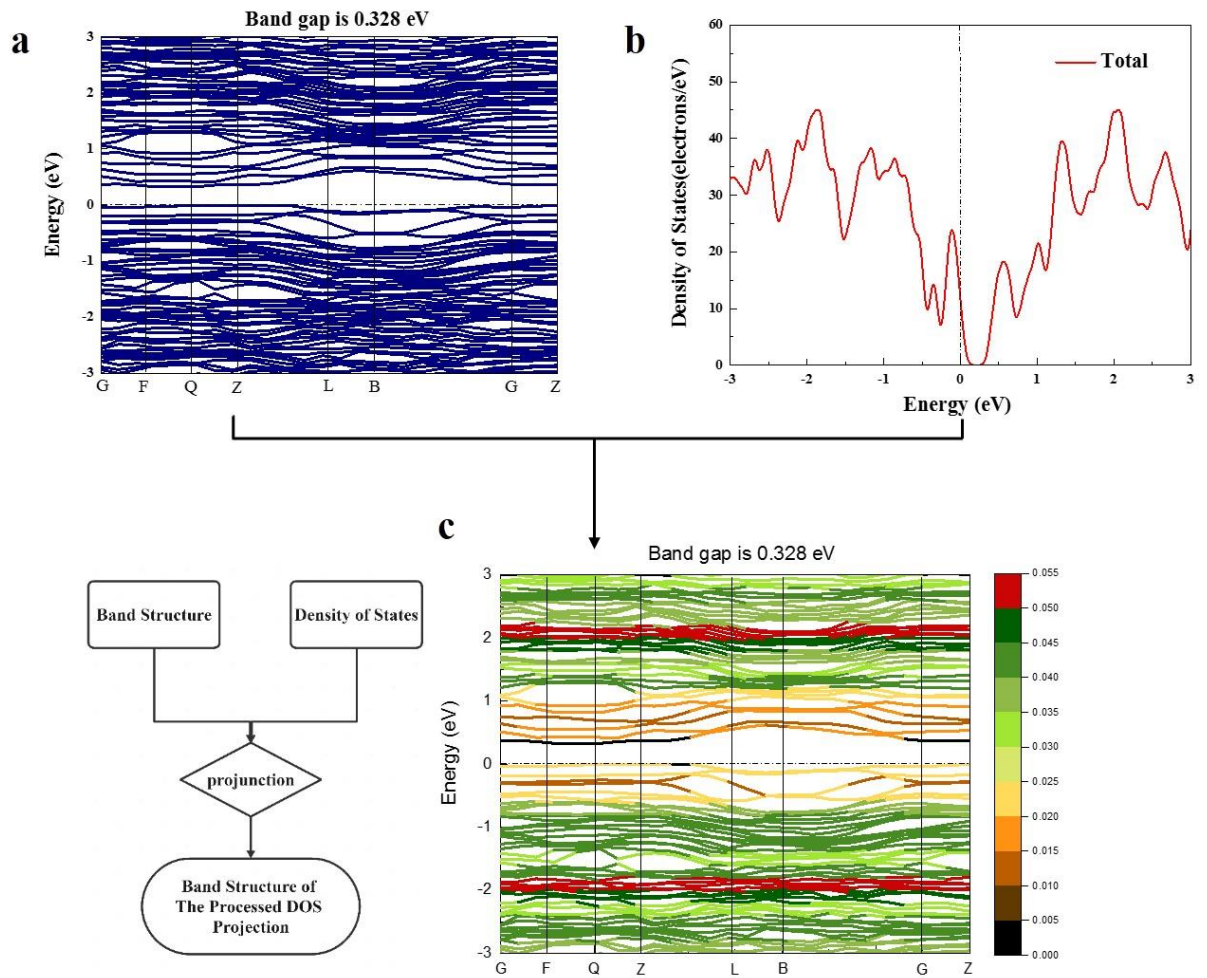


Fig. 6 Projection flow chart; (a) band structure, (b) total density of states, and (c) band structure of the processed DOS projection.

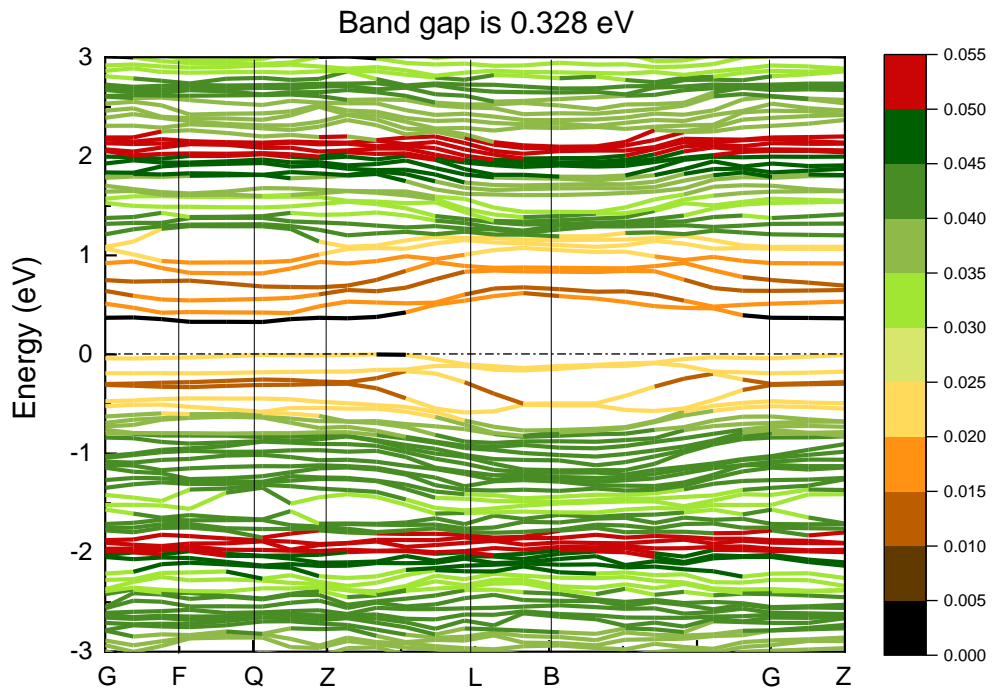


Fig. 7 Band structure of the processed DOS projection. Colors closer to black and red represent a lower and higher probability, respectively, that the electrons appear in the corresponding energy range on the path of the Brillouin zone.

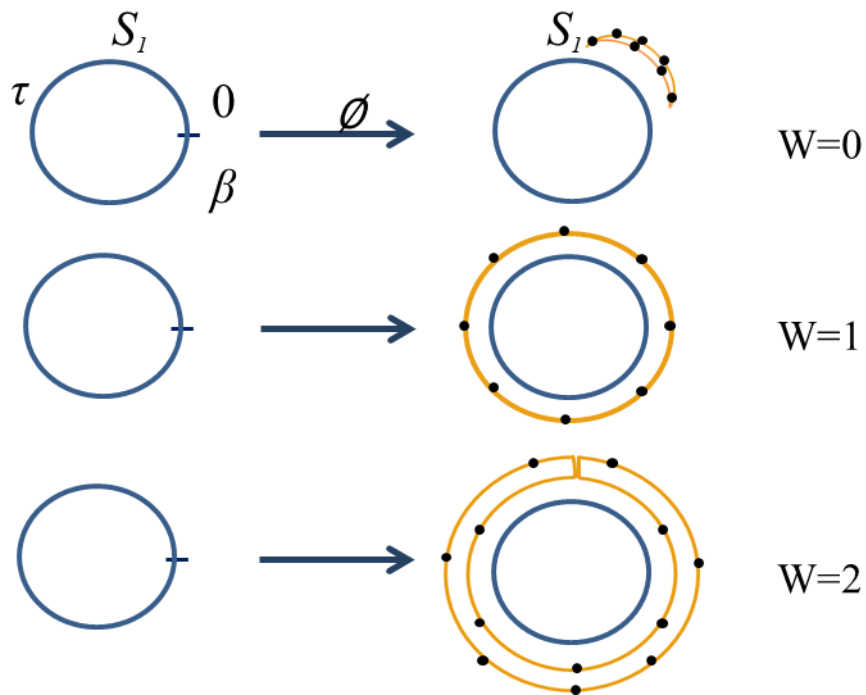


Fig. 8 Mappings $\phi: S_1 \rightarrow S_1$ of different winding numbers (W).

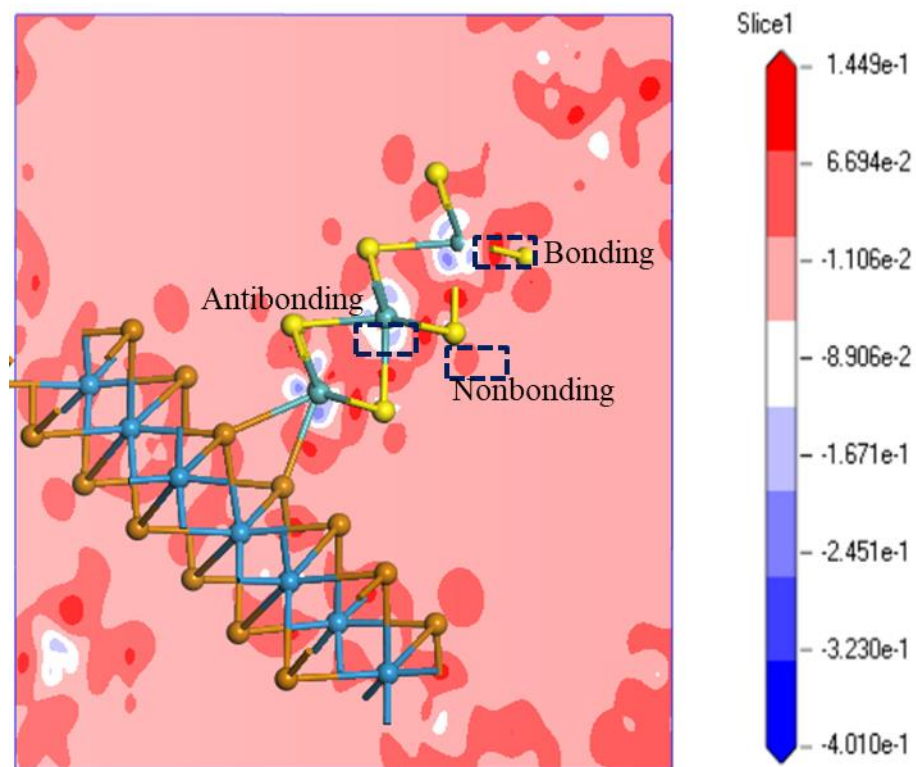


Fig. 9 Deformation charge density of WTe_2/MoS_2 heterostructure.

Table 1 Lattice parameters of T-type WTe₂/MoS₂ heterostructure.

Structure	Angle			Lattice parameter (Length)		
	α (deg)	β (deg)	γ (deg)	a (Å)	b (Å)	c (Å)
WTe ₂ /MoS ₂	90.00	90.00	76.10	6.235	12.980	14.638

Table 2 T-type WTe₂/MoS₂ heterostructure atomic fractional coordination after optimization.

Atom	x	y	z
Te1	0.687	0.000	0.111
Te2	0.114	0.140	0.101
Te3	0.548	0.280	0.099
Te4	0.972	0.426	0.109
Te5	0.398	0.574	0.110
Te6	0.827	0.719	0.099
Te7	0.254	0.859	0.101
W8	0.338	0.000	0.229
W9	0.786	0.148	0.230
W10	0.232	0.274	0.227
W11	0.628	0.418	0.226
W12	0.044	0.582	0.226
W13	0.505	0.726	0.227
W14	0.935	0.851	0.230
Te15	0.686	0.000	0.347
Te16	0.116	0.140	0.355
Te17	0.541	0.281	0.357
Te18	0.974	0.422	0.334
Te19	0.396	0.577	0.334
Te20	0.823	0.718	0.358
Te21	0.257	0.859	0.355
Mo22	-0.025	0.504	0.501
Mo23	0.479	0.496	0.501
S24	0.284	0.373	0.556
S25	0.795	0.372	0.555
S26	0.168	0.627	0.556
S27	0.657	0.627	0.556
Mo28	0.228	0.500	0.678
Mo29	0.728	0.499	0.678
S30	0.041	0.375	0.742
S31	0.541	0.373	0.739
S32	0.418	0.624	0.743
S33	0.914	0.626	0.739
Mo34	-0.022	0.503	0.863
Mo35	0.481	0.495	0.863

S36	0.287	0.375	0.924
S37	0.789	0.372	0.921
S38	0.162	0.626	0.922
S39	0.663	0.623	0.925

Table 3 Probability of the energy range and corresponding color.































Probability(Integral value)	Energy range	Color
0.038	(-3.0 eV ~ -2.8 eV)	
0.040	(-2.8 eV ~ -2.6 eV)	
0.041	(-2.6 eV ~ -2.4 eV)	
0.035	(-2.4 eV ~ -2.2 eV)	
0.046	(-2.2 eV ~ -2.0 eV)	
0.053	(-2.0 eV ~ -1.8 eV)	
0.042	(-1.8 eV ~ -1.6 eV)	
0.030	(-1.6 eV ~ -1.4 eV)	
0.041	(-1.4 eV ~ -1.2 eV)	
0.042	(-1.2 eV ~ -1.0 eV)	
0.042	(-1.0 eV ~ -0.8 eV)	
0.037	(-0.8 eV ~ -0.6 eV)	
0.020	(-0.6 eV ~ -0.4 eV)	
0.013	(-0.4 eV ~ -0.2 eV)	
0.023	(-0.2 eV ~ 0.0 eV)	
0.003	(0.0 eV ~ 0.2 eV)	
0.001	(0.2 eV ~ 0.4 eV)	
0.014	(0.4 eV ~ 0.6 eV)	
0.018	(0.6 eV ~ 0.8 eV)	
0.019	(0.8 eV ~ 1.0 eV)	
0.023	(1.0 eV ~ 1.2 eV)	
0.043	(1.2 eV ~ 1.4 eV)	
0.034	(1.4 eV ~ 1.6 eV)	
0.037	(1.6 eV ~ 1.8 eV)	
0.046	(1.8 eV ~ 2.0 eV)	
0.050	(2.0 eV ~ 2.2 eV)	
0.035	(2.2 eV ~ 2.4 eV)	
0.037	(2.4 eV ~ 2.6 eV)	
0.042	(2.6 eV ~ 2.8 eV)	
0.030	(2.8 eV ~ 3.0 eV)	

Table 4 Chemical bonding states, deformation charge density $\Delta\rho_i(r_{ij})$, and potential functions $V_{cry}(r_{ij})$ of the van der Waals heterojunctions obtained using the calculated bond charge ($\epsilon_0 = 8.85 \times 10^{-12} C^2 N^{-1} m^{-2}$, $e = 1.60 \times 10^{-19} C$)

Mo/S ($r_{ij}=d/2=2.407/2 \text{ \AA}$)	
$\Delta\rho^{hole}(r_{ij}) (e/\text{\AA}^3)$	-4.010×10^{-1}
$\Delta\rho^{bonding-electron}(r_{ij}) (e/\text{\AA}^3)$	1.449×10^{-1}
$\Delta\rho^{nonbonding-electron}(r_{ij}) (e/\text{\AA}^3)$	6.694×10^{-2}
$\Delta\rho^{antibonding-electron}(r_{ij}) (e/\text{\AA}^3)$	-8.906×10^{-2}
$V_{cry}^{nonbonding}(r_{ij})(eV)$	-0.976
$V_{cry}^{bonding}(r_{ij})(eV)$	-2.112
$V_{cry}^{Antibonding}(r_{ij})(eV)$	1.298

References

- [1] J. Bonde, P. G. Moses, T. F. Jaramillo, J. K. Nørskov, I. Chorkendorff, *Faraday Discuss.*, **2009**, 140, 219-231.
- [2] A. Litke, T. Weber, J. P. Hofmann, E. J. M. Hensen, *Appl. Catal., B*, **2016**, 198, 16-24.
- [3] T. A. Pecoraro, R. R. Chianelli, *J. Catal.*, **1981**, 67, 430-445.
- [4] H. Ning, Y. Zeng, S. Zuo, S. V. Kershaw, Y. Hou, Y. Li, X. Li, J. Zhang, Y. Yi, L. Jing, J. Li, M. Gao, *ACS Nano*, **2021**, 15, 873-883.
- [5] X. Huang, J. Tang, B. Luo, R. Knibbe, T. Lin, H. Hu, M. Rana, Y. Hu, X. Zhu, Q. Gu, D. Wang, L. Wang, *Adv. Energy. Mater.*, **2019**, 9, 1901872.
- [6] J. He, K. Hummer, C. Franchini, *Phys. Rev. B*, **2014**, 89, 075409.
- [7] J. Zhang, L. Zhang, X. Ma, Z. Ji, *Appl. Surf. Sci.*, **2018**, 430, 424-437.
- [8] F. Ullah, Y. Sim, C. T. Le, M.-J. Seong, J. I. Jang, S. H. Rhim, B. C. Tran Khac, K.-H. Chung, K. Park, Y. Lee, K. Kim, H. Y. Jeong, Y. S. Kim, *ACS Nano*, **2017**, 11, 8822-8829.
- [9] F. Ceballos, M. Z. Bellus, H.-Y. Chiu, H. Zhao, *ACS Nano*, **2014**, 8, 12717-12724.
- [10] C. Yelgel, Ö. C. Yelgel, O. Gülseren, *J. Appl. Phys.*, **2017**, 122, 065303.
- [11] Y. Guo, J. Robertson, *Appl. Phys. Lett.*, **2016**, 108, 233104.
- [12] D. Gu, X. Tao, H. Chen, W. Zhu, Y. Ouyang, Y. Du, Q. Peng, *Phys. Stat. Sol. RRL*, **2020**, 14, 1900582.
- [13] J. Shim, D.-H. Kang, Y. Kim, H. Kum, W. Kong, S.-H. Bae, I. Almansouri, K. Lee, J.-H. Park, J. Kim, *Carbon*, **2018**, 133, 78-79.
- [14] C. J. Cramer, D. G. Truhlar, *Phys. Chem. Chem. Phys.*, **2009**, 11, 10757-10816.
- [15] F. Steglich, S. Wirth, *Rep. Prog. Phys.*, **2016**, 79, 084502.
- [16] J. Heyd, G. E. Scuseria, M. Ernzerhof, *J. Chem. Phys.*, **2003**, 118, 8207-8215.
- [17] J. Liao, B. Sa, J. Zhou, R. Ahuja, Z. Sun, *J. Phys. Chem. C*, **2014**, 118, 17594-17599.
- [18] S. Peredkov, S. L. Sorensen, A. Rosso, G. Öhrwall, M. Lundwall, T. Rander, A. Lindblad, H. Bergersen, W. Pokapanich, S. Svensson, O. Björneholm, N. Mårtensson, M. Tchapyguine, *Phys. Rev. B*, **2007**, 76, 081402.
- [19] A. E. Cocke, P. Z. Fulé, J. E. Crouse, *Int. J. Wildland Fire*, **2005**, 14, 189-198.
- [20] M. C. Payne, M. P. Teter, D. C. Allan, T. A. Arias, J. D. Joannopoulos, *Rev. Mod. Phys.*, **1992**, 64, 1045-1097
- [21] A. Mohajeri, M. Alipour, *Chem. Phys.*, **2009**, 360, 132-136.
- [22] M. Omar, Elementary solid state physics: principles and applications, *Addison-Wesley*, **1993**.
- [23] M. Bo, H. Li, Z. Huang, L. Li, C. Yao, *AIP Adv.*, **2020**, 10, 015321.
- [24] M. Bo, H. Li, A. Deng, L. Li, C. Yao, Z. Huang, C. Peng, *Mater. Adv.*, **2020**, 1, 1186.
- [25] C. Q. Sun, Theory:BOLS and NEP, in C.Q. Sun (Ed.) *Relaxation of the Chemical Bond: Skin Chemisorption Size Matter ZTP Mechanics H2O Myths*, Springer Singapore, Singapore, **2014**, pp.203-221.
- [26] M. Bo, L. Li, Y. Guo, C. Yao, C. Peng, C. Q. Sun, *Appl. Surf. Sci.*, **2018**, 427, 1182-1188.